



**POLITECNICO  
DI TORINO**



**Université  
de Paris**

Master's double degree in Nanotechnologies and Quantum Devices

Master's Thesis

# Characterization and design of quantum cascade detectors for mid-Infrared radiation.

Characterization of the experimental setup for responsivity measurements and quantum engineering of an optimal architecture for future generation of devices.

## **Supervisors**

Prof. Carlo Ricciardi

Prof. Maria Luisa Della Rocca

## **Candidate**

Federico Plazzotta

## **Supervisor**

**III-V Lab**

Dr. Alexandre Delga

July 2020

## **Abstract**

Quantum cascade detectors are intersubband devices that offer bright prospects for photodetection of mid-Infrared radiations because of high detection speed, reliable room temperature operation and excellent Johnson noise limited detectivity. This is achieved thanks to the photovoltaic operating principle allowed by their design, comprising an internal potential gradient in the form of a quantum cascade, hence the name of the devices. In this work, the experimental setup to measure the spectral responsivity of such photodetectors is described, together with all aspects of their physics. Moreover the improvement of device performance and the investigation of an optimal architecture in terms of detectivity are discussed, relying on the key concept of quantum engineering of the bandstructure.

# Acknowledgements

In the first place I wish to express my gratitude to my supervisor, Dr. Alexandre Delga: he defined the objectives of my internship and supported me with patience and transparency, while allowing me to develop my work independently at the same time. I am also grateful for the trust he placed in me by allowing me to work in the lab from day one, and for the clarity of his explanations on scientific matters.

I must thank Dr. Jean-Luc Reverchon, the head of the "Mid-IR" group, for his efforts in making sure I had everything I needed to continue my work during these particular months of teleworking, and for giving me the opportunity to attend the group meetings.

For what concerns the practical aspects of the work I wish to mention the help received from Dr. Virginie Trinité and Mathurin Lagree in providing me access to the simulation tools and introducing me to their use. I also appreciated very much the help of Gregory Quinchard and Thomas Poletti, who watched after me during the first days in the laboratory.

I must also recognize the merits of the academic institutions I attended, Politecnico di Torino and Université Paris Diderot, which prepared me in the best way for such internship.

I would like to extend my thanks to my family, my parents and my brother, for supporting me in every choice I made. The patience they had towards the grumpy side of my temper is unique, and certainly it was very much appreciated.

Finally I must acknowledge the continuous support I received from my girlfriend and my longtime friends. Their joyful company in video-calls made the writing of this thesis carefree and fun, despite the quarantine.

# Contents

<b>List of Figures</b>	III
<b>List of Symbols</b>	IV
<b>1 Introduction</b>	1
1.1 State of the art . . . . .	1
1.2 Presentation of the laboratory and of the research group . . . . .	3
1.3 Motivations and objectives . . . . .	4
1.4 Organization of the report . . . . .	4
<b>2 Photoresponsivity spectrum</b>	5
2.1 Experimental setup . . . . .	6
2.2 Circuit transfer function . . . . .	8
2.3 Leakage capacitance . . . . .	9
<b>3 Quantum engineering of QCD at <math>4\mu m</math></b>	12
3.1 Intersubband transitions in quantum wells . . . . .	13
3.2 Physics of QCD . . . . .	14
3.2.1 Electronic transport . . . . .	14
3.2.2 Noise . . . . .	16
3.3 Optimal bandstructure for QCDs at $4\mu m$ . . . . .	17
3.3.1 Introduction to the software . . . . .	17
3.3.2 Choice of the period structure . . . . .	18
3.3.3 Single period optimization . . . . .	20
<b>4 Conclusions and perspectives</b>	24
<b>A Confined electronic states</b>	25
A.1 Finite quantum well . . . . .	26

# List of Figures

1.1	State of the art of QCD performances . . . . .	3
2.1	Patch antennae architecture of the QCDs under test . . . . .	5
2.2	Experimental setup for responsivity measurements . . . . .	6
2.3	Amplified photocurrent spectra . . . . .	7
2.4	Equivalent electrical circuit model of the experimental setup . . . . .	8
2.5	Fitting of photocurrent spectra, showing the low pass behaviour of the TIA . . . . .	9
2.6	Frequency behaviour of experimental setup, and signal to noise ratio . . . . .	10
2.7	Leakage capacitance investigation: photocurrent spectra and fitting procedure. . . . .	10
3.1	Architecture of a period in a QCD . . . . .	15
3.2	Schematics of self-consistent solver for transport problem . . . . .	17
3.3	Responsivity dependence on temperature and material system . . . . .	19
3.4	Optimal bandstructures quantum engineered exploiting Metis simulator . . . . .	20
3.5	Escape probability, noise and detectivity for different bandstructures . . . . .	22
3.6	Double resonant tunnel extraction scheme . . . . .	23
A.1	Graphical representation of the computation to obtain the energy levels in a finite quantum well . . . . .	26

# List of Symbols

$\mathcal{D}^*$	Detectivity
$\mathcal{R}$	Responsivity
$\lambda$	Wavelength
$w$	Wavenumber
$\nu$	Radiation frequency
$\omega$	Angular frequency
$\eta_{ext}$	External quantum efficiency
$\eta_{abs}$	Absorption efficiency
$f_{scanner}$	Scanning frequency of FTIR mirror
$R_{sh}$	QCD shunt resistance
$R_s$	QCD series resistance
$C_j$	QCD junction capacitance
$G$	TIA gain
$\omega_{-3dB}$	TIA cutoff angular frequency
$R_i$	TIA input resistance
$C_i$	TIA input capacitance
$Z_{in}$	TIA input impedance
$I_{QCD}$	Photogenerated current
$C_w$	Connection cable capacitance
$C_l$	Leakage capacitance
$\Psi_{n,\nu}$	Electron wavefunction
$\mathbf{p}$	Electron momentum
$\mathbf{e}$	Radiation polarization vector
$A$	Photodetector surface
$p_e$	Escape probability
$R_0$	QCD differential resistance
$\mathcal{D}_J^*$	Johnson specific detectivity
$i_{noise,J}^2$	Johnson noise current spectral density
$n_s$	Doping density
$N$	Number of periods
$E_{LO}$	Longitudinal optical phonon energy

# Chapter 1

## Introduction

Quantum cascade detectors (QCDs) are optoelectronic devices capable of absorbing light through intersubband transitions (ISB) between electronic states confined in semiconductor heterostructures. Their birth in 2004 [1] follows the development of previous ISB optoelectronic technologies; the quantum well infrared photodetector (QWIP) and the quantum cascade laser (QCL). ISB photodetectors have been a topic of high scientific and practical interest for more than three decades, particularly because they provide the possibility of quantum engineering the electronic bandstructure of the device through design. Moreover they allow the detection of photons with energy lower than the semiconductor bandgap, and consequently QCDs are particularly suited for applications in the mid-Infrared and terahertz range of the electromagnetic spectrum.

The motivation behind the development of the QCD arises from the need of reducing dark current noise, which is the main noise source in photoconductive QWIPs. For this purpose the structure is designed in order to provide an internal potential gradient, allowing unilateral transport of the photogenerated carriers along a cascade of electronic states, without any external bias. However, thanks to bandstructure engineering, photodetection in QCDs is possible with any bias, allowing a further degree of freedom in the research of the optimal operating condition.

The main interest in the mid-Infrared wavelength range relies on the atmospheric windows at 3–5  $\mu m$  and 8–10  $\mu m$ , within which losses due to absorption from the molecules of the atmosphere are strongly reduced. This, combined with the intrinsic speed of such devices, makes QCDs interesting for applications in spectroscopy and space communications.

The reduced electrical noise of QCDs allows room temperature operation for 3–5  $\mu m$  detection, but is still characterized by an insufficiently high device resistance at high temperatures, which limits the operating conditions for longer wavelength detection. As a consequence, despite having the promising features mentioned above, QCDs are still not widely diffused out of research laboratories, also due to the competition of interband detectors showing higher temperature operation and detectivity.

### 1.1 State of the art

Detection of infrared light relies both on thermal and photonic detectors. The former exploit the heating of the active region, induced by the interaction with the optical beam, to sense the incident radiation by measuring any temperature dependent property. Photodetectors instead convert photons into electrons and measure the current induced by the photogenerated carriers flowing between the external contacts.

In general the latter provide higher sensitivity and faster response time, but are detrimentally affected by thermal noise. They can absorb photons thanks to interband or intersubband transitions, depending on whether the initial and final state of the excited electron lay in

different bands or not. As a consequence the range of wavelengths detectable by interband detectors is constrained by the energy gap between the conduction and valence band, while ISB devices are capable of detecting photons with energies lower than the semiconductor bandgap. Moreover intersubband detectors can be designed for a wide range of wavelengths using a single material system, by accurately engineering the semiconductor layer thicknesses.

The realization of the first QCDs is dated 2004 [1], but the development of such work can be seen as the evolution of a previous study [2], which analysed the behaviour of quantum cascade laser structures exploited as photodetectors. The newborn technology consisted of lattice-matched III-V heterostructures. It was characterized by photoresponse lower than that of the more mature QWIP, but presented comparable absorption efficiency and reduced dark current noise despite its primitive design.

In the following years research developed to satisfy different purposes and in terms of improved performances in the mid-IR and at longer wavelengths. In the last two decades several studies have been published presenting new functionalities such as broadband [3] and normal incidence photodetection through coupling with surface plasmons [4]. New architectures have been developed, improving photoresponse thanks to enhanced coupling of the quantum wells [5], or increasing the extraction efficiency of the photogenerated carriers exploiting a diagonal transition scheme [6]. Quantum cascade detectors have been demonstrated over a wide range of wavelengths, from mid-IR to terahertz, and working temperatures, but they all have in common the strong dependence of performances on the architecture. Research shows that an optimal structure can be designed according to the desired application, but in most cases this implies a tradeoff between figures of merits that cannot coexist.

In order to characterize the behaviour of a QCD it is necessary to define a figure of merit capable of considering the effectiveness of device absorption, transport and the resistance to noise. Such metric is the specific Detectivity  $\mathcal{D}^*$ , which estimates the sensitivity of a photodetector, independently on the operational bandwidth and the detector surface. It is defined for a radiation of frequency  $\nu$ , as the normalization of the Noise Equivalent Power (NEP) with respect to area ( $A$ ) and bandwidth ( $\Delta f$ ). NEP is the impinging optical power required to photo-generate a signal of intensity equal to noise current  $i_n$ , as shown in Eq.1.1.

$$\mathcal{D}^*(\nu) = \frac{\sqrt{A \cdot \Delta f}}{NEP} = \frac{\mathcal{R}(\nu) \cdot \sqrt{A \cdot \Delta f}}{i_n} \quad \text{Jones} = \frac{cm \cdot \sqrt{Hz}}{W} \quad (1.1)$$

where  $\mathcal{R}$  identifies Responsivity, the ratio between the photocurrent exiting the detector and the optical power generating it, as

$$\mathcal{R} = \frac{I}{P_{opt}} \quad \text{expressed in } \frac{A}{W} \quad (1.2)$$

Fig.1.1 resumes the best results achieved for QCDs according to the publication year, the detected wavelengths and material systems used. The figure of merit used to compare the performances of such different devices is defined as FOM:

$$FOM = \frac{\mathcal{D}^*}{\lambda} \sqrt{T} \cdot e^{\frac{hc}{2\lambda k_B T}} \quad (1.3)$$

This expression normalizes specific detectivity by wavelength,  $\lambda$ , and thermal activation of dark noise,  $\sqrt{T} \cdot exp$ , giving a relevant quantity to compare photodetectors operating at different temperatures and detection energies.

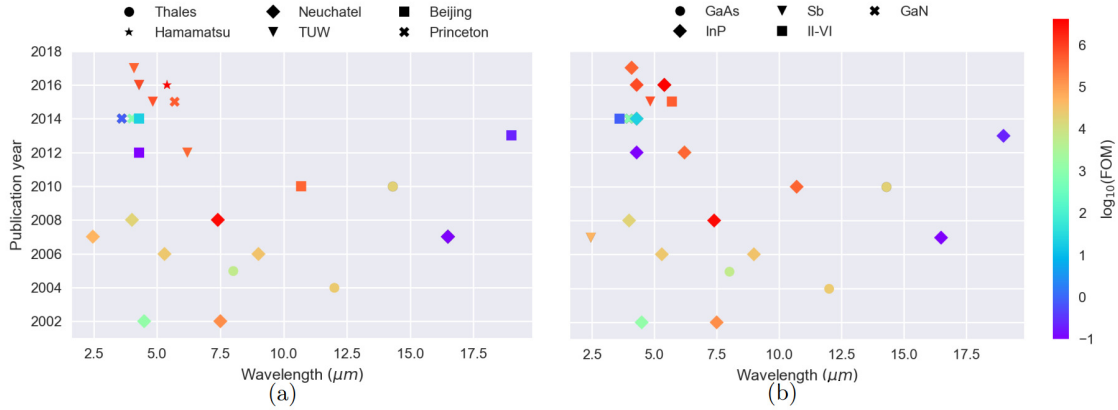


**Figure 1.1:** State of the art of QCD performance (FOM is presented in Eq.1.3) as function of wavelength. Particular focus on the group involved (a), and the materials used (b), images from[7].

## 1.2 Presentation of the laboratory and of the research group

The work presented in this report has been developed in the group directed by Dr. Jean-Luc Reverchon at III-V Lab. The latter is a private research laboratory set-up between Thales, Nokia and CEA/Leti, and is one of the most important industrial research laboratories in Europe for the development of III-V semiconductors technologies and their integration with Silicon circuits. The purpose of the research activity is that of creating the state of the art of new technologies in the fields of wireless networks and communications, aerospace and defence by working at the core of systems.

The activity of the "Mid-IR" group is centred on the realization of Quantum Cascade Detectors (QCDs) for mid-Infrared wave detection. Particular focus is paid to the developing of optimal designs to improve the performances of the photodetector [8], and to the analysis of the physical phenomena which govern the behaviour of the device [7]. Great efforts are also dedicated to the understanding of the physics of superlattices and to strong light-matter coupling. The theoretical research activity is supported by experimental work, consisting in the characterization and in the analysis of the response of the QCD, fabricated according to the previously designed model. In other words, the work of the group is not just focused on the improvement of an existing device, but covers all the aspects of its realization from the core of the technology.

### 1.3 Motivations and objectives

In accordance with the plans of the group, the work presented in this report has the goal of characterizing the experimental setup to analyse the responsivity spectrum of a QCD, which was fabricated and designed in order to provide detection at  $10\ \mu\text{m}$ . The research on this technology is motivated by the increasing demand of high-speed photodetectors for future communications of data through the atmosphere [9].

Moreover it was decided to focus the research work on designing an optimal structure for a QCD detecting at  $4\ \mu\text{m}$ . The objective is to propose an efficient design dedicated to the  $3 - 5\ \mu\text{m}$  atmospheric window, inspired by the most innovative architectures for longer wavelength detection [5; 6], and by mature strain-compensated lattice technology [10; 11; 12]. The latter investigation is a preliminary study for a possible thesis project dedicated to  $4\ \mu\text{m}$  detection.

### 1.4 Organization of the report

This thesis is structured according to the different objectives addressed during the work, and to the theoretical notions necessary to understand the discussion. Chapter 2 presents in detail the experimental setup used for the characterization of the optical response of a first generation of QCDs detecting at  $10\ \mu\text{m}$ . Particular attention will be paid to the frequency behaviour of the circuit and to the definition of its transfer function by analysis and fitting of the experimental data.

In chapter 3 QCDs are analysed from a theoretical point of view, and the quantum engineering of the bandstructure is investigated exploiting Metis software simulations. The discussion begins with an overview of the physics of intersubband transitions, reported in section 3.1, and continues in section 3.2 focusing on the physical mechanisms and on the figures of merit which rule the behaviour of the device. The theoretical concepts described in these sections will be finally applied in section 3.3 to engineer an optimal architecture for a QCD detecting at  $4\ \mu\text{m}$ .

A summary of this work and its perspectives are reported in chapter 4, followed by the detailed calculation of the electronic states in a structure having one confined dimension, illustrated in Appendix A.

# Chapter 2

## Photoresponsivity spectrum

This chapter has the purpose of describing the experimental activity conducted in the laboratory, whose objective was the characterization of an optoelectronic setup for measuring the spectral responsivity of QCDs.

The devices under test were the result of the work of a PhD student of the group<sup>1</sup>, who designed and fabricated them in order to detect at  $10\ \mu m$ . They were realized according to a patch antennae architecture, as shown in Fig.2.1, where the active region of each detector is embedded between two metallic layers. This structure realizes a metal-semiconductor-metal cavity where the top patch is an antenna, allowing to capture photons from a collective area larger than the electrical surface defined by the patch size. It is important to note that this architecture makes QCDs sensitive to normal incidence radiations<sup>2</sup>, and allows to design patches with reduced surface without detrimentally affect absorption of photons. Small electrical area is a desirable feature for patches as it provides low parasitic capacitance that, together with the intrinsic fast response-time guaranteed by intersubband transition mediated by phonons, provides photodetectors with large cutoff frequencies and high speed.

In accordance with the expectations, preliminary investigations on such devices led to the conclusion that this first generation of QCDs is able to provide very fast detection, but is characterized by low photoresponse. The work described in this chapter started in such context, and aimed at designing the optimal experimental setup for the analysis of the photodetector responsivity.

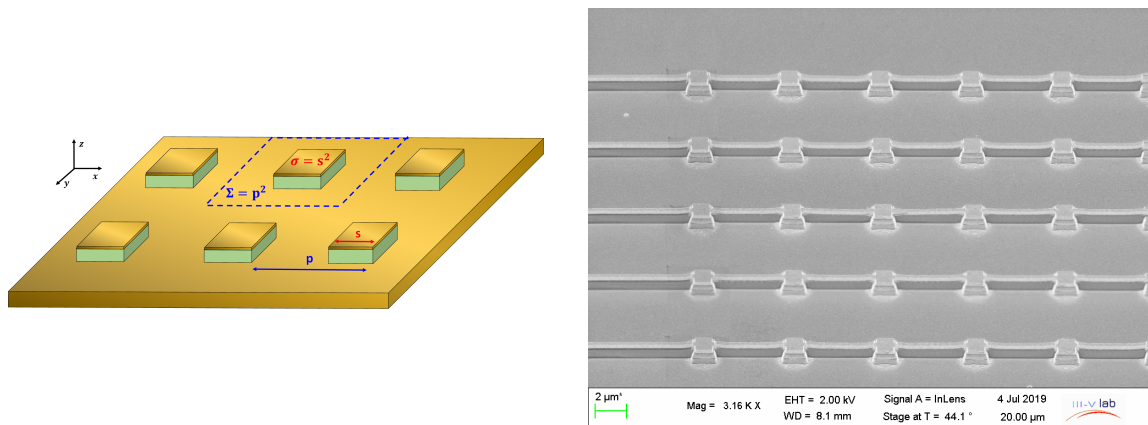


**Figure 2.1:** (a) Graphical representation of patch-antenna resonators, image from [15], and (b) scanning electron microscopy image<sup>1</sup> of the QCDs under test.

<sup>1</sup>Credits to Gregory Quinchart.

<sup>2</sup>ISB transitions are otherwise sensitive only to light polarized along the heterostructure growth axis.

## 2.1 Experimental setup

As it is known that temperature affects the device performance in a detrimental way, the sample holding the QCDs was placed inside a cryostat working at  $77\text{ K}$ , and every detector was contacted with an external pin in order to measure the electrical response.

Light is provided by a Globar source, a blackbody emitting radiation over a wide spectrum of wavelengths, located inside a *Bruker Vertex 70* Fourier Transform Interferometer (FTIR). In the latter, the radiation is directed towards a Michelson interferometer, where the beam is split and recombined after following paths of different lengths thanks to a movable mirror. This generates interference of the two beams, thus leading to modulation of the source radiation resulting in different wavelengths according to mirror position. The QCDs are characterized by narrow absorption linewidth and consequently, when the modulated radiation impinges on them, they generate an AC photocurrent whose frequency is related to the oscillation frequency of the movable mirror of the interferometer.

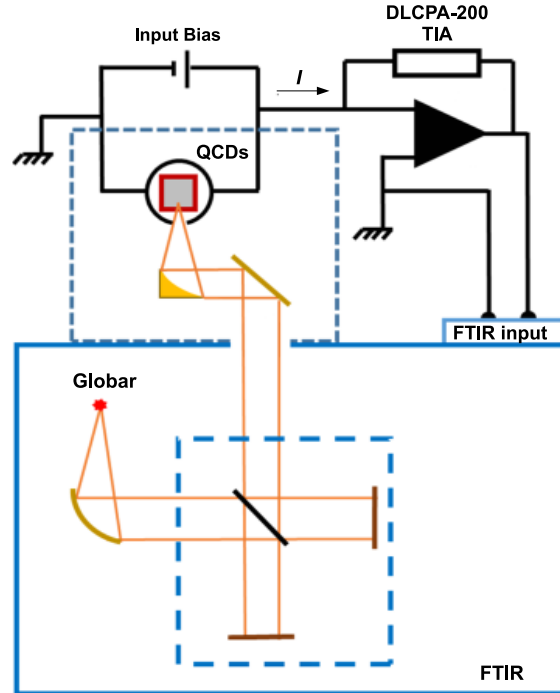


**Figure 2.2:** Experimental setup for responsivity measurements, image adapted from [15].

The photocurrent generated by the QCD is very small in amplitude and buried in noise. In order to extract usable informations, the signal is amplified thanks to a low noise trans-impedance amplifier (TIA, model *DLPCA-200*), which is characterized by a low input impedance and provides a voltage proportional to the current flowing to its terminals. The amplified signal is then directed back towards the FTIR where a digital signal processor (DSP), which acts as a lock-in amplifier, demodulates the amplified signal giving as a result the spectral response of the device. The experimental setup is shown in Fig.2.2.

The process of demodulation essentially consists in the mixing of the input signal with a reference signal through a frequency mixer, thus allowing to extract a signal from a noisy environment.

Such operations, together with the alignment of the optical periscope to direct the beam towards the QCDs, led to the results reported in Fig.2.3, where the spectra for several oscillation frequencies of the mirror  $f_{\text{scanner}}$  are shown. The signal to noise ratio (SNR) of such spectra can be deduced from the logarithmic scale plots reported in the insets<sup>3</sup>. Different incident wavelengths correspond to different wavenumbers  $w$ , which are related to temporal frequencies in the electrical signal via:

$$f = w \cdot \frac{f_{\text{scanner}}}{15798.2} \quad (2.1)$$

where the scanning frequency of the FTIR is normalized with respect to the frequency of the interferogram signal from the reference laser, commonly a HeNe-laser emitting at  $15798,2 \text{ cm}^{-1}$  [13].

From these spectra is already clear that the TIA has low pass amplification, consequently the choice of  $f_{\text{scanner}}$  leads to a tradeoff between the time required to generate the spectrum and the gain of the amplifier. In fact the photogenerated spectra are obtained faster for larger oscillation frequencies of the FTIR mirror, but this regime may be above the cutoff frequency defining the response of the circuit. In order to define the best operation frequency the transfer function of the system was derived and its frequency response was analysed.

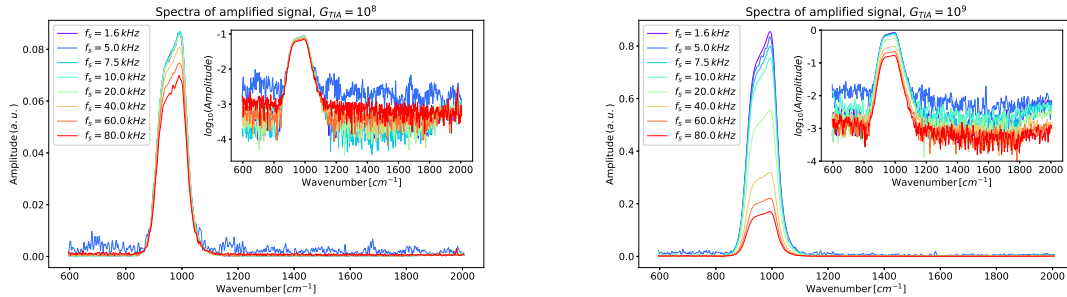


**Figure 2.3:** Photovoltage spectrum for amplifier gain  $G = 10^8 \text{ V/A}$  (a), and  $G = 10^9 \text{ V/A}$  (b) in arbitrary units. The logarithmic scale is reported in the inset to highlight signal to noise ratio.

<sup>3</sup>It is clear at first sight that the FTIR operating at  $f_{\text{scanner}} = 5 \text{ kHz}$  generates a noise one order of magnitude higher than the others.

## 2.2 Circuit transfer function

In order to model the QCD the conventional picture of photodiodes is exploited, according to which a photodetector can be described by a current source in parallel with a shunt resistance  $R_{sh}$ , and a junction capacitance  $C_j$ . The shunt resistance in a QCD is a figure of merit strongly dependent on temperature and, as for the other photodetectors, it is defined as the inverse slope of the current-voltage curve in dark conditions and at zero bias. Thanks to I-V measurements previously made by the group, I could estimate  $R_{sh} \simeq 1,55 M\Omega$  at  $77 K$ . The photodetector model also exploits a series resistance  $R_s$  to model the ohmic behaviour of the contacts. However it has not been considered in the following calculation as its value is usually around tens of  $\Omega$ , negligible with respect to the input impedance  $Z_{in}$  of the TIA connected in series, which is characterized by a resistor  $R_i$  in parallel to a capacitor  $C_i$ .

The TIA exploited in the experiment cannot be modeled as an operational amplifier with a feedback consisting of a resistor in parallel with a capacitor. In fact it consists of a cascade of gain stages with compensation circuits in between, and as a consequence it has to be modelled as a black-box having the transfer function reported in 2.2

$$H(s) = \frac{G}{1 + \frac{1}{\omega_{-3dB}}s} \quad (2.2)$$

where  $G$  is the gain of the amplifier expressed in  $V/A$  and  $\omega_{-3dB}$  is the upper cutoff frequency of the TIA reported on the datasheet. Thus the complete setup can be modelled as in Fig.2.4, where  $C_w$  is the capacitance of the cables and  $C_l$  is the capacitance modelling the circuit leakage that will be discussed in next section.

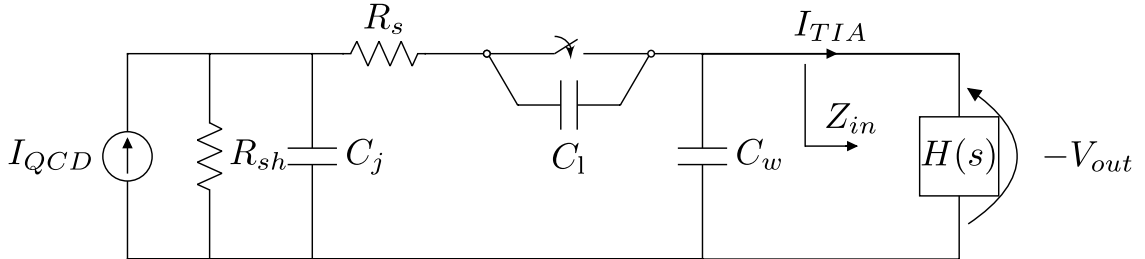


**Figure 2.4:** Equivalent electrical circuit model for the transimpedance behaviour of the experimental setup. The switch is closed when the setup is correctly short-circuited.

The transfer function of the circuit was evaluated considering the partition of the current photogenerated by the detector  $I_{QCD}$  as shown in Eq.2.3

$$-V_{out} = I_{TIA} \cdot H(s) \quad \text{and} \quad I_{TIA} = \frac{R_{sh} \parallel \frac{1}{s(C_j + C_w)}}{(R_{sh} \parallel \frac{1}{s(C_j + C_w)}) + (R_i \parallel \frac{1}{sC_i})} \cdot I_{QCD} \quad (2.3)$$

where  $I_{TIA}$  is the current flowing into the terminals of the amplifier. The above equations lead to the expression of the circuit transfer function presented below:

$$-V_{out} = I_{QCD} \cdot \frac{G \cdot \omega_{-3dB}}{\omega_{-3dB} + s} \cdot \frac{R_{sh}(1 + sR_iC_i)}{sR_{sh}R_i(C_i + C_j + C_w) + R_{sh} + R_i} \quad (2.4)$$

$I_{QCD}$  and  $C_j$  are the only unknowns of the latter equation, thus the amplitudes extracted from the signal spectra were fitted with such expression in order to find the best possible estimation of such parameters. The fitting procedure, graphically shown in Fig.2.5, allowed to estimate the value of  $I_{TIA}$  in arbitrary units, while it was of no help in the definition of the detector capacitance.

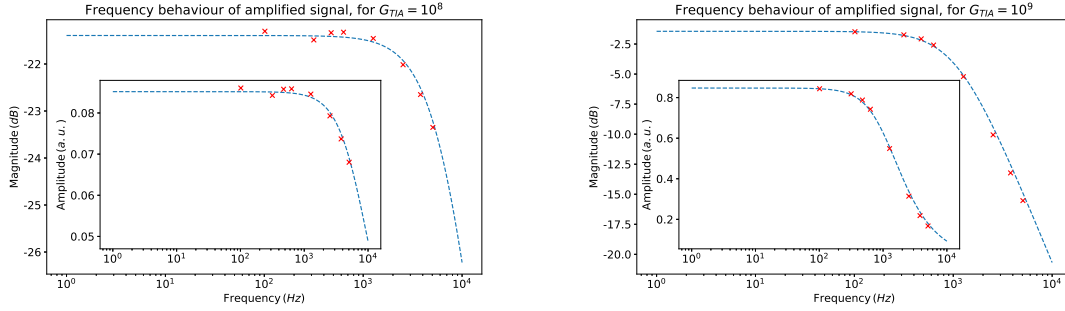


**Figure 2.5:** Low-pass behaviour of TIA amplifier. Fitting of the experimental data for signal amplified with  $G = 10^8$  V/A (a), and  $G = 10^9$  V/A (b).

This is due to the low input impedance of the transimpedance amplifier<sup>4</sup>, which makes the transfer function of Eq.2.4 insensitive to the variation of  $C_j$  in the range of frequencies span by the FTIR modulation. In fact the transfer function can be rewritten with good approximation as a first-order low pass filter, whose bandwidth is ruled by the TIA cutoff frequency as shown in Eq.2.5.

$$-V_{\text{out}} = I_{QCD} \cdot \frac{G \cdot \omega_{-3\text{dB}}}{\omega_{-3\text{dB}} + s} \quad (2.5)$$

The cutoff frequency of such transfer function is ruled by the gain of the amplifier, defining the tradeoff between bandwidth and amplitude of the transfer function, as shown in Fig.2.6a. The choice of the latter also influences the signal to noise ratio and consequently, according to the results reported in Fig.2.6b, it is convenient to operate at the highest possible amplification to maximize such figure of merit.

### 2.3 Leakage capacitance

During the experimental work described above it was noted that the circuit was providing a signal even when the common contact of the QCDs was not shortcircuited with the cryostat shell (ground). Ideally the spectra obtained in this "open circuit" configuration is expected to be flat, but the experimental results reported in Fig.2.7a show a peak in detection at the right wavelength. As a consequence the existence of a leakage capacitance  $C_l$  between cryostat and common contacts of the patch was hypothesised, as shown in Fig.2.4.

<sup>4</sup>Amplifier input impedacen is however high enough to make series resistance negligible, as  $R_i$  is of the order of  $k\Omega$ .

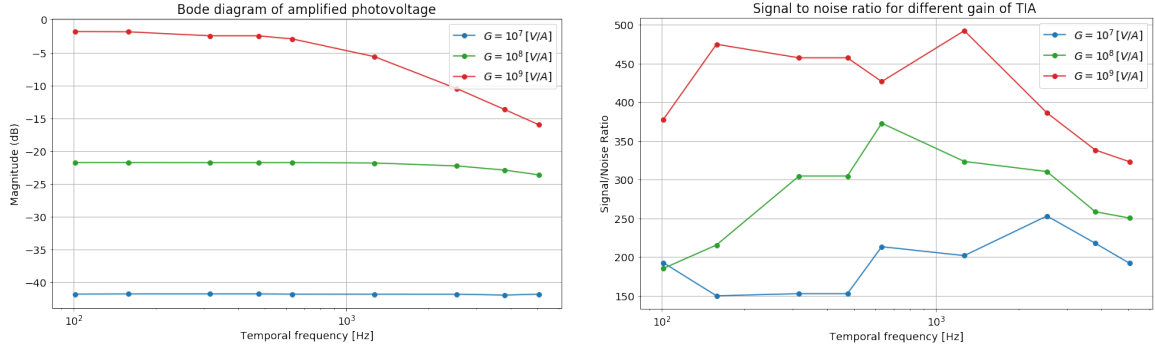


**Figure 2.6:** Bode diagram (a), and signal to noise ratio (b), of photovoltage for different gains.

Such leakage may appear irrelevant for what concerns the transmission of the signal, but it is of great relevance when considering the noise.

The transfer function of this circuit was evaluated similarly to the case reported in previous section, leading to Eq.2.6, and it was used to fit the experimental data in order to extract the value of the leakage capacitance. The computation, whose graphical outcome is shown in Fig.2.7b, allowed to estimate the value of the leakage capacitance  $C_l \simeq 110 \text{ pF}$ <sup>5</sup>.

$$-V_{\text{out}} \simeq I_{QCD} \cdot \frac{G \cdot \omega_{-3\text{dB}}}{\omega_{-3\text{dB}} + s} \cdot \frac{sC_l R_{sh}}{s^2 [C_l C_j R_i R_{sh}] + s [R_i C_l + R_{sh} (C_j + C_i)] + 1} \quad (2.6)$$

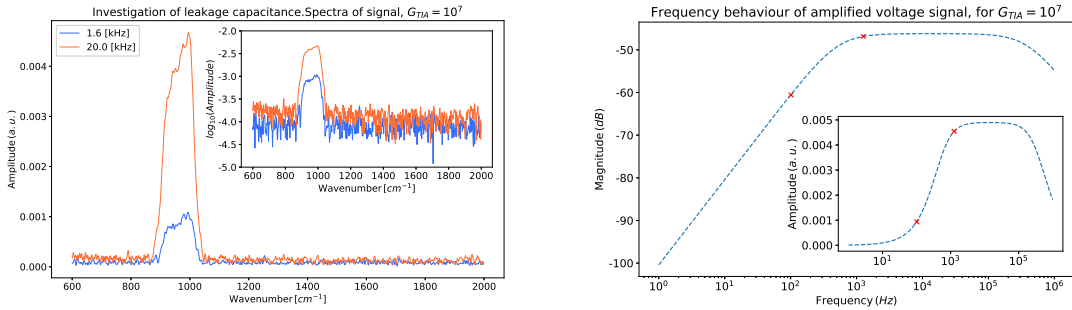


**Figure 2.7:** Leakage investigation. (a) Experimental data for signal amplified with  $G = 10^7 \text{ V/A}$  and (b) fitting of experimental data, resulting in the estimation of  $C_l$ .

<sup>5</sup>The value of the photocurrent generated,  $I_{QCD}$ , is the same of previous computations, as the detector is in both cases under the same illuminating and operating conditions.

The few experimental spectra taken into account for the latter analysis are justified by the fact that the experimental work in the laboratory had to stop suddenly according to the security guidelines due to the pandemic<sup>6</sup>. The following step in the characterization of an optimal circuit would have been the introduction of a voltage source to bias the QCDs, and a more detailed analysis of the best amplifier configuration in term of signal to noise ratio. Moreover it was in the plans to further investigate and fix the capacitive leak, and to normalize the measured photocurrent spectrum by the spectral distribution of the global source, thus allowing to extract the intrinsic spectral dependency of the device responsivity.

Unfortunately the experimental work had to stop at this point, and consequently the efforts were directed towards bibliography, theoretical aspects and simulations of QCD architectures as explained in the following chapter.

---

<sup>6</sup>The data exploited for the leakage analysis were initially discarded because taken without properly closing the circuit (open circuit in Fig.2.4), their physical relevance was reconsidered during teleworking when it was impossible to acquire more data.

## Chapter 3

# Quantum engineering of QCD at $4\ \mu\text{m}$

Intersubband detectors for mid-Infrared wavelengths have been developed in order to provide a cheap and material integrated alternative to commercial interband detectors based on Mercury Cadmium Telluride. Room temperature operation is fundamental for any optoelectronic technology aiming to provide low-cost systems, and QCDs can be designed to efficiently operate in such conditions thanks to reduced electrical noise. Moreover they provide interesting features such as low background noise, high speed detection, architecture flexibility and, especially in the mid-IR range, they can rely on mature technology for what concerns the processing methods of semiconductor materials. Different material systems can be exploited to fabricate the active region, and lattice-matched heterostructures are not the only solution. Strain-compensated structures [11; 12] exploit different composition of the alloys characterizing the heterostructure, allowing to engineer the depth of the quantum well providing a better coverage of the atmospheric window.

The variety of possible architectures and materials systems makes QCDs promising for different applications such as spectroscopy, sensing of  $CO_2$  and free space optical communications in the atmospheric window. Each application has particular requirements in terms of detection speed, responsivity and thermal resistance and consequently the bandstructure of the device needs to be engineered to achieve optimal performances according to the different needs.

The purpose of this chapter is to set the guidelines to design an optimal architecture for a room temperature QCD detecting around  $4\ \mu\text{m}$ . The formalism related to the eigenfunctions of electrons confined in a quantum well is important for the understanding of the following chapter, but such concepts are generally well known, and consequently they are reported in [Appendix A](#). The first two sections of this chapter are thought to provide a brief, but comprehensive, overview of the physical phenomena ruling the behaviour of a quantum cascade detector. Theoretical notions regarding intersubband transitions are reported, followed by the discussion on electronic transport and noise reported in the second section. Finally, in the third section the focus is on the quantum engineering of the QCD bandstructure, highlighting the effects that the architecture of the device has on its performance. These concepts will be investigated with the help of theoretical simulations relying on Metis software, in order to study which architecture leads to highest detectivity. This study has to be considered as a preliminary work for the fabrication and characterization of such devices, which would be the topic of a following PhD.

### 3.1 Intersubband transitions in quantum wells

Quantum wells (QW) heterostructures are made by the periodic repetition of layers characterized by different energy gap. In the practical case of QCDs the structure is based on the alternation of III-V semiconductors, such as InGaAs/InAlAs, whose conduction band offset (CBO) gives rise to confinement of electronic states along the growth direction, resulting in splitting of the conduction subbands. The latter have parabolic dispersion curves almost parallel to each other; their confinement energy difference defines the detectable photon energy, and thus the wavelength operation of the QCD.

Absorbing light means transforming the incoming photon energy into excitation energy of an electron which, as a consequence, is promoted to a higher energy level. The light-matter interaction Hamiltonian  $\hat{H}_{int}$  can be derived from the expression of the electromagnetic wave to be detected and is equal to<sup>1</sup>:

$$\hat{H}_{int} = \frac{ie\mathcal{E}_0}{2m^*\omega} \mathbf{e} \cdot \mathbf{p} \quad (3.1)$$

where  $\mathbf{p}$  is the momentum of the electron,  $\mathbf{e}$  is the polarization vector,  $e$  is the electronic charge,  $\mathcal{E}_0$  is the amplitude of the electric field and  $\omega$  is the radiation frequency. Light-matter interaction in QW is studied exploiting Fermi's golden rule, which allows to calculate the transition rate from an initial state  $i$ ,  $|\Psi_{n,\nu}\rangle$ , to a final state  $f$ ,  $|\Psi_{n',\nu'}\rangle$  under the effect of the interaction Hamiltonian  $\hat{H}_{int}$ , as shown in Eq.3.3.

$$W_{ij}(\omega) = \frac{2\pi}{\hbar} \left| \langle \Psi_{n',\nu'} | \hat{H}_{int} | \Psi_{n,\nu} \rangle \right|^2 \delta(E_f - E_i - \hbar\omega) \quad (3.2)$$

$$\propto |\langle \Psi_{n',\nu'} | \mathbf{e} \cdot \mathbf{p} | \Psi_{n,\nu} \rangle|^2 \delta(E_f - E_i - \hbar\omega) \quad (3.3)$$

In order to study the matrix element  $|\langle \Psi_{n',\nu'} | \mathbf{e} \cdot \mathbf{p} | \Psi_{n,\nu} \rangle|$  it is useful to rewrite the electronic wavefunction exploiting the envelope function approximation, leading to the following expression:

$$\Psi_{n,\nu}(\mathbf{r}) = u_\nu(\mathbf{r}) \cdot f_n(\mathbf{r}) \quad \text{with} \quad f_n(\mathbf{r}) = \frac{e^{i\mathbf{k}_{xy} \cdot \mathbf{r}}}{\sqrt{A}} \cdot \psi_n(z) \quad (3.4)$$

where  $f_n(\mathbf{r})$  is defined as the slowly varying envelope function. Now the matrix element of Eq.3.3 can be expanded as:

$$|\langle \Psi_{n',\nu'} | \mathbf{e} \cdot \mathbf{p} | \Psi_{n,\nu} \rangle| = \mathbf{e} \cdot \langle u_{\nu'} | \mathbf{p} | u_\nu \rangle \langle f_n | f_{n'} \rangle + \mathbf{e} \cdot \langle u_\nu | u_{\nu'} \rangle \langle f_n | \mathbf{p} | f_{n'} \rangle \quad (3.5)$$

The first term of Eq.3.5 identifies interband transitions, while the second refers to optical intersubband transitions as it is non-zero only for states belonging to the same band  $\nu = \nu'$ . It is interesting to expand the latter term exploiting the definition of the envelope function reported in Eq.3.4.

$$\mathbf{e} \langle f_n | \mathbf{p} | f_{n'} \rangle = \frac{1}{A} [e_x \hbar p_x + e_y \hbar p_y] \delta_{n',n} \delta_{k'_{xy},k_{xy}} + \frac{1}{A} \cdot e_z \delta_{k'_{xy},k_{xy}} \int dz \psi_n^*(z) p_z \psi_{n'}(z) \quad (3.6)$$

---

<sup>1</sup>This expression is true when considering the radiation Gauge and if dipole approximation is valid. The full derivation can be found in [15].

Recalling that the considered matrix element is part of the transition rate of Eq.3.3, the above equation defines the two selection rules for intersubband transitions. First, a photon can be absorbed only if its energy leads to an electronic transition between levels of different parity<sup>2</sup>. Most importantly, only the term proportional to the polarization of the radiation along the  $z$  axis is relevant when  $n \neq n'$ , leading to the fact that only light polarized along the growth direction of the heterostructure gives rise to intersubband transitions. These calculations are essential in the context of intersubband photodetectors, and motivate why QCDs are insensitive to radiations having polarization parallel to the quantum wells characterizing the heterostructure.

## 3.2 Physics of QCD

Detection is the combination of two physical processes, absorption of photons and successive transport of the photogenerated carriers, and both mechanisms must be optimized to improve photodetector performance. QCDs in particular are unipolar devices whose active region is characterized by the repetition of the same structure, also called period (see Fig.3.1a). Each period is characterized by at least one n-doped well, where the absorption of photons happens through bound-to-bound transitions of electrons between two confined subbands. The upper level of the optically active quantum well is coupled to a cascade extractor: a succession of QWs, designed in order to unilaterally drive the photogenerated electrons towards the ground state of the next period. The repetition of this mechanism along the whole structure results in a current flowing between the electrical contacts at the extremities of the device.

The number of electrons flowing in the external circuit for each impinging photon defines the external quantum efficiency  $\eta_{\text{ext}}$ . It is usually more interesting to express this quantity in terms of currents and optical power rather than fundamental particles, leading to the definition reported in Eq.3.7

$$\eta_{\text{ext}} = \frac{N_e}{N_p} = \mathcal{R} \frac{\hbar\omega}{\lambda} = \mathcal{R} \frac{hc}{\lambda e} \quad (3.7)$$

where  $\mathcal{R}$  is the previously defined Responsivity.

### 3.2.1 Electronic transport

Electronic transport in QCDs is treated exploiting a 1D model of transport along the growth direction, while carriers are treated as free in the in-plane axis. This model considers subbands to be in thermal quasi-equilibrium, because of the fast electron-electron scattering happening with timescales  $\tau_{th} \simeq 200\ \text{fs}$  [9]. As a consequence, the confined states are treated as reservoirs exchanging electrons according to transition rates depending on design and operating conditions.

When an electron is photoexcited from the ground state of the optical QW, it can either jump back to the initial level (denoted by 0 in Fig.3.1a) or tunnel through the barrier

---

<sup>2</sup>  $\int dz \psi_n^*(z) p_z \psi_{n'}(z) \neq 0$  only if  $\psi_n^*(z)$  and  $\psi_{n'}(z)$  have different parity.

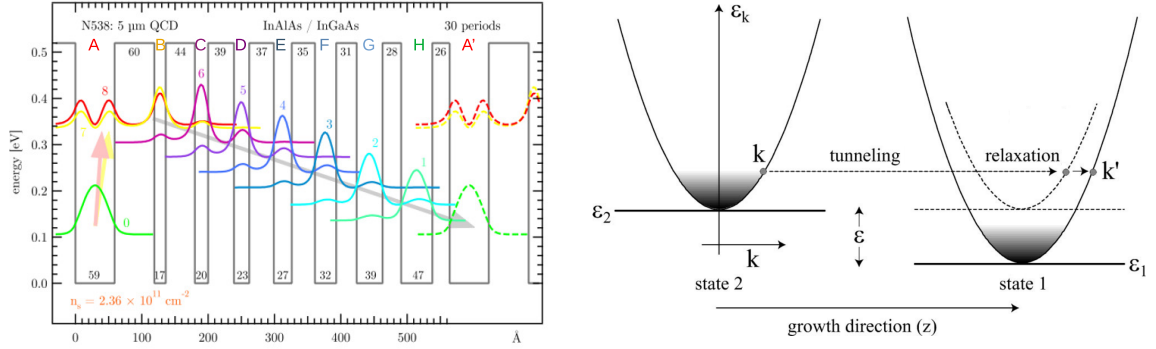


**Figure 3.1:** (a) Calculated conduction band profile, and moduli squared of the Wannier-Stark wavefunctions for a QCD detecting at  $5\ \mu\text{m}$ , image adapted from [16]. (b) Tunneling in the picture of localized subbands, image adapted from [15].

into the first well of the cascade extractor. In the latter case the carrier hops towards the successive state of the cascade, labeled as 6, by a double-step process: tunneling through the barrier and emission of a longitudinal optical (LO) phonon. Transport in QCDs is usually treated according to Wannier-Stark formalism as illustrated in Fig. 3.1a, where the delocalization of the wavefunction over adjacent wells allows hopping of the photogenerated carriers along the cascade extractor.

The extractor is designed in order for the intersubband scattering to be repeated until the electron reaches the ground state of the optical well of the next period. This mechanism provides a displacement of charge along the whole structure and consequently generates a current measurable by an external circuit. The escape probability  $p_e$  can be defined as the fraction of photogenerated electrons that reach the next period of the cascade thanks to efficient extraction. In order to maximize  $p_e$ , the scattering rates of the transitions driving the electrons inside the cascade must be maximized with respect to backscattering or recombination via LO-phonon emission into the ground state of optical well of the period. This is done quantum engineering the barrier thicknesses and the wells widths characterizing each period of the device, considering that the scattering rate of LO-phonons is in good approximation proportional to the overlap integral (OI) of the participating energy levels [6].

Intersubband scattering has typical time scale of the order of  $ps$ , thus legitimating the picture of thermalized subbands, and also providing an explanation for the very high speed of QCDs. In fact the time response of a photodetector is determined by the transit time of the electrons through the active region which, in the case of QCDs, would give rise to cutoff frequencies of the order of  $100\ \text{GHz}$ . In practice this range of frequencies is not reached as time response is also limited by the stray inductance of the wires and the parasitic capacitance of the detector, proportional to its surface. For this reason the QCDs analysed in chapter 2 rely on a patch antennae architecture, as it allows to minimize the parasitic capacitance thus shifting damping towards higher frequencies.

The efficiency of transport inside a QCD can be defined in terms of the number of electrons flowing through the device contacts for each photon absorbed, thus introducing the internal quantum efficiency:

$$\eta_i = \frac{p_e}{N} \quad (3.8)$$

where  $N$  is the number of periods of the active region. This allows to express the external quantum efficiency as an explicit function of the efficiencies of the two processes ruling detection, photon absorption  $\eta_{\text{abs}}$  and transport of photogenerated electrons  $\eta_i$ :

$$\eta_{\text{ext}} = \frac{N_e}{N_p} = \eta_{\text{abs}} \cdot \eta_i \quad (3.9)$$

All these quantities are included in the definition of responsivity as shown in Fig.3.10.

$$\mathcal{R} = \frac{\lambda e}{hc} \eta_{\text{abs}} \frac{p_e}{N} \quad (3.10)$$

The influence of the number of periods on the performance of the device is a relevant issue to be considered when designing a QCD architecture, and it will be addressed in detail in the next sections.

### 3.2.2 Noise

When analysing device performances noise needs to be taken into account as it inevitably affects every measurement process. The most relevant contributions to current noise in the context of III-V intersubband photodetectors are shot noise and Johnson noise, both originating from scattering of quantized charges. Johnson term provides the dominant noise contribution close to equilibrium conditions, in the limit provided by  $eV \ll k_B T$ , and consequently it is the main noise mechanism in photovoltaic devices operating at high temperature such as QCDs.

In a device of differential resistance  $R_0$ , current spectral density due to Johnson noise is defined as in Eq.3.11:

$$i_{\text{noise},J}^2 = \frac{4k_B T \Delta f}{R_0} \quad (3.11)$$

which shows how, particularly for QCDs detecting at room temperature, a large differential resistance is necessary to minimize noise. The latter equation allows to rewrite the expression of specific detectivity reported in Eq.1.1 as follows:

$$\mathcal{D}_J^*(\nu) = \mathcal{R}(\nu) \sqrt{\frac{R_0 A}{4k_B T}} \quad (3.12)$$

where  $A$  is the surface of the detector.

Eq.3.12 defines Johnson noise detectivity, which provides informations about responsivity, transport efficiency and resistance to noise. As a consequence it is the most complete figure of merit for analysing QCD performance, and the simulation work described in next section had the final goal of maximizing such quantity.

### 3.3 Optimal bandstructure for QCDs at $4\ \mu\text{m}$

This section is dedicated to the theoretical simulations performed to design an optimal architecture of a QCD operating at room temperature around  $4\ \mu\text{m}$ . Several parameters, each targeting a particular physical phenomenon, influence the performance of QCDs. Often different requirements cannot coexist and so the structure has to be engineered according to the specific application it is designed for.

In the following discussion the effect of doping, number of periods, wells widths and barrier thicknesses will be analysed, with particular focus on the quantum engineering of the bandstructure by tuning the wells widths and the barriers thicknesses to maximize detectivity (Eq.3.12).

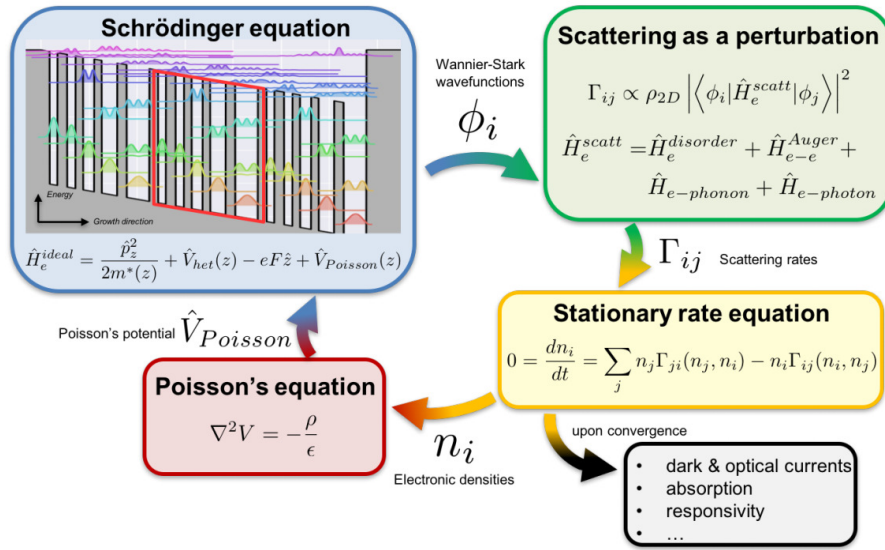


**Figure 3.2:** Schematics of the self-consistent method solving transport problem, image from [7].

#### 3.3.1 Introduction to the software

The simulations were performed exploiting Metis, a software developed by the group, which self-consistently solves the transport problem for a given input architecture. First of all it finds the electronic wavefunctions solving Schrödinger's equation, then it computes the scattering rates induced by the perturbation Hamiltonian<sup>3</sup>. This allows to obtain the electronic densities by imposing the stationary rate equation, thus allowing to compute Poisson's potential. The latter contributes to the input potential and so the computation is performed cyclically with the updated potential value until a self consistent solution is obtained as shown in Fig.3.2.

<sup>3</sup>The perturbation Hamiltonian defines transitions due to photon absorption, phonon scattering and disorder of the lattice.

The computation of the rate equations is performed exploiting Wannier Stark hopping, which provides good results when evaluating intersubband transitions whose detuning is large, but overestimates the rates of the transitions happening between resonant states. This leads to correct estimation of the scattering rates between subbands of the cascade extractor, separated roughly by the energy of a LO phonon, while it is inappropriate to describe the resonant tunneling process happening between the optical well and the first well of the cascade.

As a consequence it is more appropriate to consider the latter transition in terms of tunneling processes (wavefunction localized in one well as in Fig.3.1b), and in the context of these simulations the choice is performed by the user according to the detuning and the coupling between the states characterizing the transition.

### 3.3.2 Choice of the period structure

The choice of the alloys characterizing the heterostructure defines the conduction band profile, and in particular it sets the energy offset between the wells and the barriers. According to the state of the art for QCDs, the most mature configuration is that of lattice matched  $\text{In}_{0.53}\text{Ga}_{0.47}\text{As}/\text{In}_{0.52}\text{Al}_{0.48}\text{As}$  heterostructure based on *InP* substrate, providing a conduction band offset about  $520\ \text{meV}$ . As the optical transition in QCDs happens between two bound states, the upper limit for the photon energy to be detected is determined by the depth of the well. As a consequence the material composition imposes a constraint on the minimum detectable wavelength, which cannot be overcome by quantum engineering. In the particular case of lattice matched  $\text{In}_{0.53}\text{Ga}_{0.47}\text{As}/\text{In}_{0.52}\text{Al}_{0.48}\text{As}$  QCDs, the minimum wavelength that can be reached is  $\lambda_D \simeq 4.3\ \mu\text{m}$ , as shown in Fig.3.3a.

In order to provide a good coverage of the  $3 - 5\ \mu\text{m}$  atmospheric window, it is thus necessary to increase the conduction band offset by exploiting strain compensated material systems. This solution allows to change the composition of the alloys constituent the heterostructure, thus allowing to modify the CBO, by careful compensating the strain induced between the barriers, quantum wells and substrate. In practice this leads to an additional constraint in designing the architecture, as the ratio between the sum of all barriers thicknesses and wells widths has to be such that the compressive strain in the QW compensates the tensile force arising in the barrier.

This constraint makes the engineering of the bandstructure more difficult, and consequently the following analysis has been conducted considering a lattice matched heterostructure of  $\text{In}_{0.53}\text{Ga}_{0.47}\text{As}/\text{In}_{0.52}\text{Al}_{0.48}\text{As}$  realized on *InP* substrate, despite room temperature detection at around  $\simeq 4.3\ \mu\text{m}$ .

Fig.3.3 provides a graphical representation of the concepts explained above, together with a demonstration of the temperature dependence of QCDs performance. An increase in temperature causes a redshift of the responsivity spectra as it influences the Fermi-Dirac distribution of electrons in the ground state of the optical well, and because of different parabolicity of the two subbands at large wave-vector states.

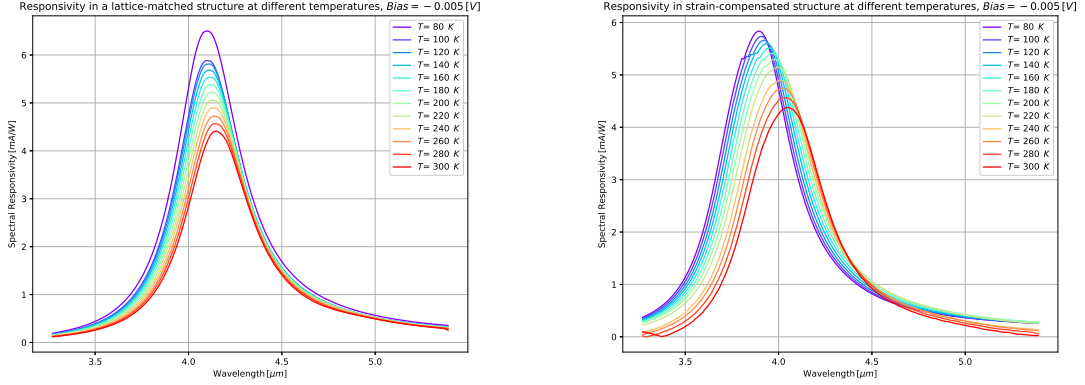


**Figure 3.3:** Temperature dependence of spectral Responsivity for the QCD of Fig.3.4b, relying on: (a) lattice-matched material system, (b) strain-compensated structure, which provides detection at lower wavelengths.

### Doping and Number of periods

Doping density  $n_s$  and number of periods  $N$  are parameters that can be engineered when designing the QCD, to maximize its detectivity. Optimal values exist, but are strongly linked with the effect that such parameters have on the absorption efficiency. As a consequence their design consists in a complex tradeoff, dependent on the electromagnetic architecture through which the field is coupled with the device active region.

The software exploited for the simulations is programmed to evaluate the response of an infinitely periodic structure, thus allowing to treat the optimization of the architecture of a single period. As a consequence the following discussion will focus on the optimization of the barrier thicknesses and the wells widths, leaving the design of doping density and number of periods to another formalism.

### Period architecture

The analysis focuses on the study of a vertical transition QCD, where the optical transition associated to detection of radiation happens between two states localized in the same quantum well (Fig.3.4). This structure was preferred to a diagonal transition architecture, which provides the advantage of reduced backscattering of the photogenerated electrons to ground state, designing the active transition to take place between two energy levels located in adjacent wells<sup>4</sup>. At short wavelengths, such as the ones considered in this context, the large optical transition energy already reduces the probability of electrons backscattering from the upper states of the cascade towards ground, thus removing the need of having a further barrier between the wells.

<sup>4</sup>At the expense of a lower responsivity due to smaller dipolar matrix element, which defines the oscillator strength ( $\propto |\langle \psi_{n'} | z | \psi_n \rangle|^2$ ).

### 3.3.3 Single period optimization

The engineering of the wells widths and barrier thicknesses is a complex task because each parameter influences transition rates and coupling between levels, thus affecting the design of the remaining elements. This gives rise to a sort of loop in which the engineering of each quantum state imposes constraints on the others, and consequently the ideal approach to face such problem is that of exploiting an optimization algorithm. The group developed an algorithm of such kind, which iteratively modifies barriers thickness and wells widths to maximize the signal to noise ratio of the structure. Such method was accessible via remote cloud only in a second time and consequently the simulations reported in the following are the result of "manual" design of the architecture according to the physics of QCDs. However the bandstructures obtained through this process are in good accordance with the optimal structures designed with the help of the algorithm, thus proving the validity of the following reasoning.

#### Quantum wells widths

The first quantity to be designed is the width of the quantum wells, as it is of fundamental relevance in defining the energy of the confined states. In fact, as introduced above, the intrinsic asymmetric potential necessary for unilateral carrier transport is achieved through a cascade of QWs with increasing thicknesses, which generates a "ladder" of energy levels. In order to provide detection around  $4.3\ \mu\text{m}$  the optical well was designed to have energy difference between the subbands of  $\simeq 300\ \text{meV}$ . The first well of the cascade extractor was then engineered to have a state resonant in energy with the excited state of the optical well, thus allowing tunneling extraction (Fig.3.4).

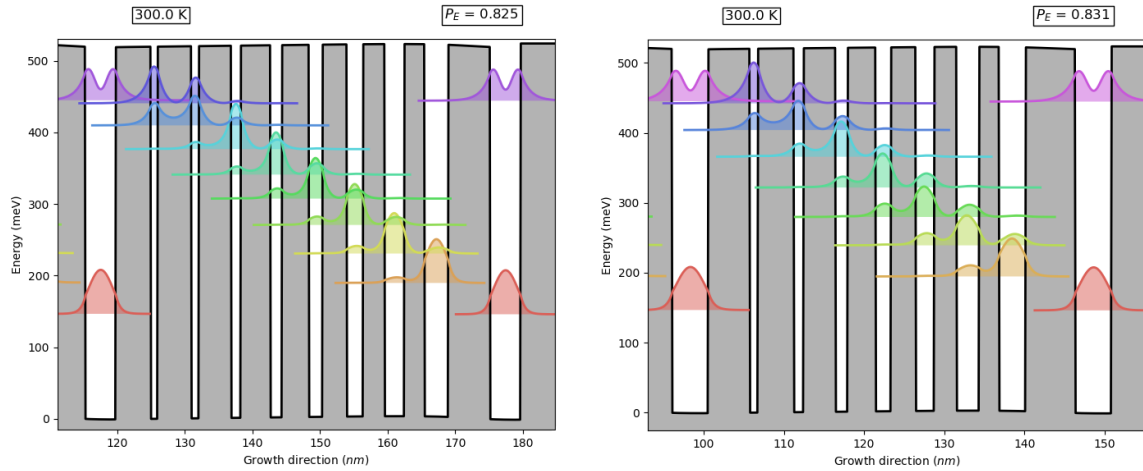


**Figure 3.4:** Period of a Quantum Cascade Detector characterized by: (a)  $\Delta E \simeq 32\ \text{meV}$ , (b)  $\Delta E \simeq 40\ \text{meV}$  resulting in an active region with one well less than the previous.

In order to achieve the fastest electronic transport through the cascade, the wells of the extractor were initially designed to provide detuning between adjacent states as close as possible to the longitudinal optical phonon energy in  $\text{In}_{0.53}\text{Ga}_{0.47}\text{As}$   $E_{LO} \simeq 32\ \text{meV}$ . This

procedure led to the architecture reported in Fig.3.4a, where each period is characterized by nine wells. The efficacy of such structure has been compared with an architecture designed with one less state in the extractor, thus showing energy difference between adjacent states to be roughly  $40\ \text{meV}$ , while keeping an optimal detuning between the first two levels of the cascade to maximize the probability of entering the extractor (Fig.3.4b). The comparison between the performances of these two architectures is discussed in the following, after a brief summary of the considerations according to which the barriers were engineered.

### Barriers thicknesses

The thickness of each barrier has to be designed considering that the photogenerated electrons must always be subject to faster transition rates towards the bottom of the cascade rather than backscattering. As a consequence the engineering of the thicknesses of the first two barriers (optical well-extractor, extractor-extractor) is the result of a competition between two transport mechanisms. In fact they need to be designed such that the photogenerated electron, after tunneling through the first barrier, hops in the second state of the cascade with higher transition rates than those characterizing the detrimental resonant-tunneling process back to the previous state. As tunneling happens at higher rate, the thickness of the barrier between optical well and extractor has to be thicker than the second one.

Moreover the widths of the barriers in the cascade extractor are engineered to be decreasing at each stage, to favour intersubband transitions assisted by phonon emission (flow towards the right in the presented images). Finally the last barrier is designed thicker than the previous to minimize the excitation of electrons from the ground level of the next period to the last well of the cascade.

In order to find the optimal values of the thicknesses of the first two barriers the detectivity of the architecture in Fig.3.4b was evaluated varying such parameters. This led to the results reported in Fig.3.5a where, as expected, the best performances are achieved for thicknesses of the optical-extractor barrier higher than the extractor-extractor barrier. However the optimal configuration seems to happen for smaller thickness differences than those usually exploited in the devices reported in literature (usually around  $10\ \text{\AA}$  [11; 10]). This can be explained considering that in our case the detuning characterizing the transition between the first two levels of the cascade is optimal for phonon mediated scattering to happen, thus providing the fastest possible extraction towards the cascade.

### Comparison between different architectures

Once these concepts are clarified it is possible to proceed with the comparison of the two architectures shown in Fig.3.4. As reported in Fig.3.5b, the noise provided by the device having larger detuning between the states of the cascade is greater. In fact in this case the levels of the extractor are closer in energy to the ground state of the optical well, thus characterizing an architecture with lower differential resistance. However the simulation results show how this difference is small when compared with respect to the changes induced by variations in thickness of the optical-extractor barrier, allowing to conclude how the differential resistance of the device is mainly ruled by the width of the latter.

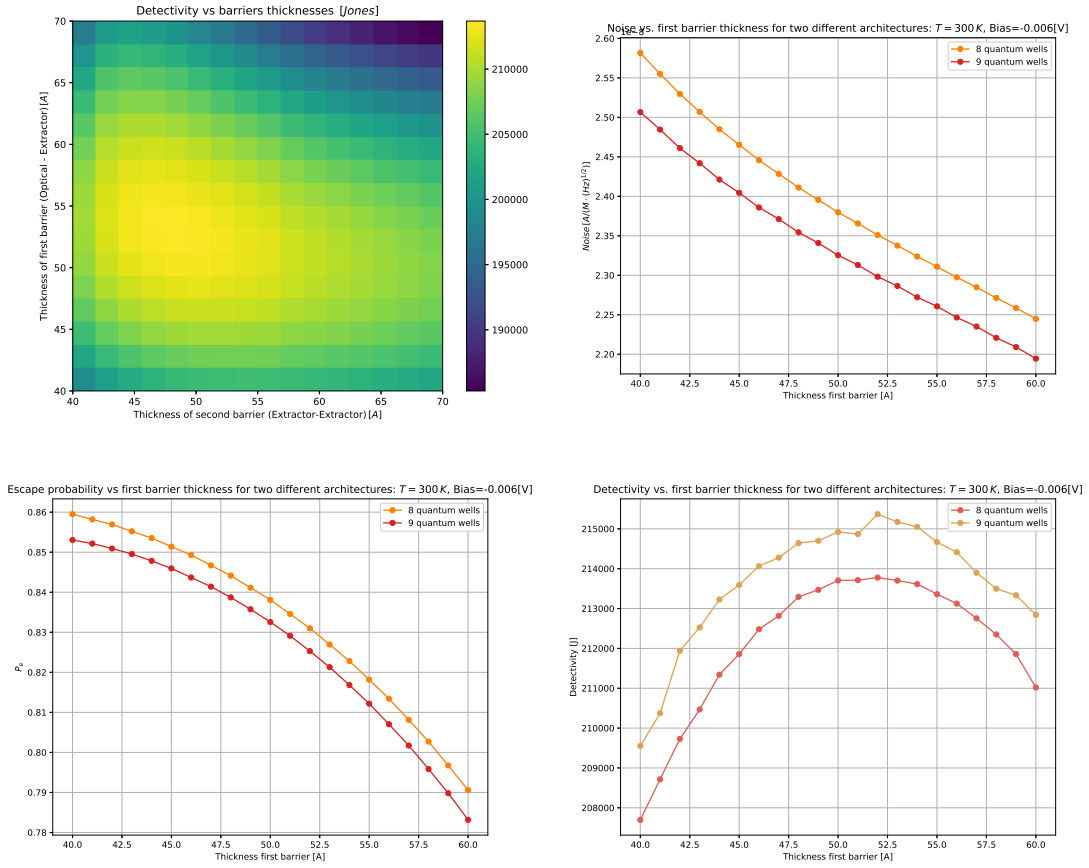


**Figure 3.5:** (a) Detectivity of the structure in Fig.3.4b for different optical-extractor and extractor-extractor barriers. Highest results achieved for  $54\ \text{\AA}$ - $48\ \text{\AA}$ . Comparison of noise (b), escape probability (c) and detectivity (d) in the two structures reported in Fig.3.4.

Moreover it is interesting to note how the escape probability of the photogenerated electrons, shown in in Fig.3.5c, can be preserved by careful designing the barriers thicknesses, even when the detuning between adjacent levels is different from the energy of the LO phonon. The above simulations showed that the differential resistance of the device is mainly ruled by the design of the first barrier, and that a cascade of states exactly spaced by  $E_{LO}$  is not essential for good performances. Moreover they show that a challenging aspect of QCD design is to maintain a high device resistance while providing high escape probability and thus responsivity. Both aspects are necessary to engineer a device with optimal performances, and the interest in a design characterized by a double resonant tunneling scheme, Fig.3.6a, arises from these concepts.

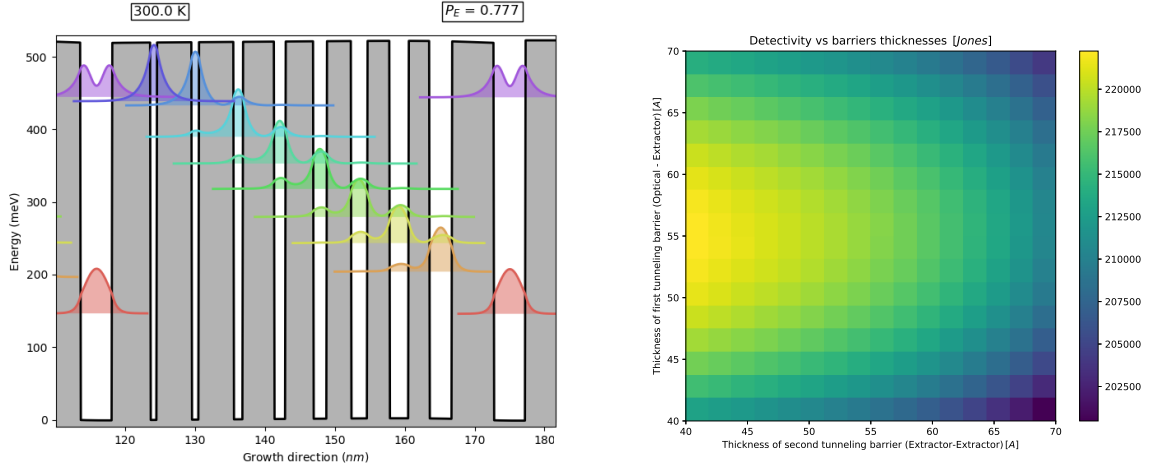


**Figure 3.6:** (a) Period of a QCD realized with a double tunnel extraction scheme (b) and its detectivity as function of the thicknesses of the barriers overcome through resonant tunneling.

In fact such architecture allows to further separate the cascade extractor from the optical well, by introducing an additional energy level resonant with the excited state of the active well. Such structure provides a high device resistance, while guaranteeing an efficient extraction scheme at the same time, resulting in improved detectivity as shown in Fig.3.6b.

The latter architecture could be further improved by designing the transition between the last well of the extractor and the ground state of the next period to exhibit a higher energy difference. This would prevent "backward" thermal excitation of electrons from the ground of the optical well, allowing to achieve better absorption efficiency, and thus responsivity, increasing device performance at higher temperature.

# Chapter 4

## Conclusions and perspectives

In the present work, the physics of quantum cascade detectors and the experimental setup designed to measure their response have been presented. The high speed and the photovoltaic operation scheme characterizing this technology make such devices extremely promising in the context of infrared detection at room temperature.

The second chapter of this manuscript has set the basis for the characterization of the experimental setup to measure the spectral responsivity of a first generation of devices. Such QCDs were characterized by high detection speed but provided a signal of small intensity, thus the procedure to amplify the photocurrent buried in noise has been reported. The collected experimental data have led to interesting considerations regarding the frequency behaviour of the circuit, and have revealed the existence of a leakage in the circuit apparatus. The main goal of near-future experimental work will be that of investigating and fixing such leakage, thus removing a detrimental feature for the measurement of the QCDs responsivity.

The third chapter has proceeded with the investigation of the defining features of QCDs from a theoretical point of view. First, the physics of intersubband transition has been reviewed, in order to comprehensively discuss the mechanisms of transport and noise in such detectors. Besides the understanding of such processes, another main point of this work has consisted in the design of an optimal period architecture, performed with the help of theoretical simulations. The quantum engineering of the bandstructure has been extremely challenging due to the mutual influence of several design parameters, and to the tradeoffs they give rise to, but has offered a direct way of manipulating the physics of the device and its performances. Several considerations have been made relying on the most innovative architectures reported in literature and on the engineering of wells and barriers, leading to the individuation of the most promising design to maximize detectivity. Such results will be further developed in the next months exploiting the SWARM optimization algorithm programmed by the group, thanks to the experience achieved in the development of the present work. The rigorous methodology that this would imply, together with the extension of the investigation towards the use of strain-compensated structures, will make the quantum engineering outcome extremely interesting and reliable for the fabrication of a future generation of devices detecting at  $4\ \mu m$ .

In a second time the thesis that will follow this work, relying on its preliminary results, will also address the engineering of the optimal electromagnetic architecture to efficiently couple the incident radiation with the active region of the device. The final ambitious goal of such research is that of providing a QCD that could be exploited in practical applications where high speed detectors are needed, such as military purposes and free space optical communications.

# Appendix A

## Confined electronic states

The following approach to determine the electronic states in a structure with one confined dimension follow the detailed calculations reported in [14]. It considers an heterostructure along  $z$  direction, while electrons are free to move in the in-plane direction ( $\mathbf{r}$ ). The starting point consists in writing the Schrödinger equation under the assumption of validity of the single band and effective mass<sup>1</sup> approximations:

$$\left[ -\frac{\hbar^2}{2m^*} \nabla^2 + V_b(z) + V_{ext}(z) \right] \Psi_{n,\nu}(\mathbf{r}) = E_{n,\nu} \Psi_{n,\nu}(\mathbf{r}) \quad (\text{A.1})$$

In the latter equation  $m^*$  is the effective mass of the confined electron,  $k$  is the carrier wavevector and  $n$  is the index identifying a subband energy level.  $V_b(z)$  is the potential given by the barrier conduction band offset and  $V_{ext}(z)$  results from externally applied fields.

The electron wavefunction  $\Psi_{n,\nu}$  can be rewritten as the product of a Bloch wavefunction  $\phi_\nu(\mathbf{r})$  and the function  $\psi_n(z)$ . The Bloch wavefunction is defined as the product between a plane-wave and the periodic function  $u_\nu(\mathbf{r})$  having the same period of the lattice structure. This reasoning allows to decouple the global motion into the free in-plane direction ( $\mathbf{r}$ ) and the confined growth direction  $z$ , leading to Eq.A.2:

$$\Psi_{n,\nu}(\mathbf{r}) = \phi_\nu(\mathbf{r})\psi_n(z) = \frac{e^{i\mathbf{k}_{xy}\cdot\mathbf{r}}}{\sqrt{A}} u_\nu(\mathbf{r})\psi_n(z) \quad (\text{A.2})$$

where  $A$  is the surface in the in plane direction, necessary to normalize the wavefunction. Thanks to the decoupling of the wavefunction the eigenenergy  $E_n$ , arising from confinement along  $z$ , can be derived from Eq.A.3a, and the total energy of each state is given by the sum of  $E_n$  with the kinetic energy of the free motion in the in-plane direction.

$$\left[ -\frac{\hbar^2}{2m^*} \frac{\partial^2}{\partial z^2} + V_b(z) + V_{ext}(z) \right] \psi_n(z) = E_n \psi_n(z) \quad E_{n,\mathbf{k}} = E_n + \frac{\hbar^2 k_{xy}^2}{2m^*} \quad (\text{A.3})$$

Considering the simplified picture where the potential barriers are infinitely high,  $V_b \rightarrow \infty$ , the eigenstates and eigenenergies in a well of width  $L$  simply become:

$$\psi_n^\infty(z) = \sqrt{\frac{2}{L}} \sin\left(\frac{\pi z}{L} \cdot n\right) \quad E_n^\infty = \frac{\hbar^2 \pi^2}{2m^* L^2} \cdot n^2 \quad (\text{A.4})$$

It is important to underline the dependence of these results on the dimensions of the well, thus on design, to remark once more the central role of quantum engineering in intersubband devices.

---

<sup>1</sup>The description of a particular state can be considered without mixing between bands, and the relevant properties of a structure come from the edges of the band, where the dispersion can be approximated as parabolic with effective mass  $m^*$ .

## A.1 Finite quantum well

The finite QW approach is more accurate for the description of real structures, and relies on the imposition of the periodic boundary conditions for both even and odd solutions. To simplify the calculations, a symmetric QW having width  $2L$  and finite barriers of potential  $V_b$  is considered, leading to even solutions of the form:

$$\psi_{n,even}(z) = \begin{cases} A \cdot e^{k(z+L)} & \text{if } z < -L \\ C \cdot \cos(hz) & \text{if } -L < z < L \\ A \cdot e^{-k(z-L)} & \text{if } z > L \end{cases} \quad (\text{A.5})$$

where  $k = \sqrt{2m_b^*(V_b - E)/\hbar}$  and  $h = \sqrt{2m_w^*E/\hbar}$ . By imposing periodic boundary conditions at  $z = \pm L$ , the following relation is obtained:

$$\frac{k}{h} = \tan(hL) \frac{m_b^*}{m_w^*} \quad (\text{A.6})$$

where  $m_b^*$  and  $m_w^*$  are the effective masses of the electron in the barrier and in the well. By defining the dimensionless quantities  $\eta = hL$  and  $\mathcal{E} = kL$  and exploiting the definition of  $h$  and  $k$  it possible to obtain the second line of equation Eq.A.7. The energy is now included in  $\eta$  and  $\mathcal{E}$ , and the allowed eigenenergies are those satisfying Eq.A.8.

$$\begin{cases} \mathcal{E} = \eta \cdot \tan(\eta) \cdot \frac{m_b^*}{m_w^*} \\ \mathcal{E} = \sqrt{2 \cdot \frac{m_b^* V_b L^2}{\hbar^2} - \eta^2 \frac{m_b^*}{m_w^*}} \end{cases} \quad (\text{A.7}) \quad \tan(\eta) = \frac{m_w^*}{\eta \cdot m_b^*} \sqrt{2 \cdot \frac{m_b^* V_b L^2}{\hbar^2} - \eta^2 \frac{m_b^*}{m_w^*}} \quad (\text{A.8})$$

Such computation was implemented exploiting the slider functionality on Python programming language, allowing to obtain the energy levels in a well as function of its width and barrier potential. Its outcome, whose graphical representation is reported in Fig.A.1a, provided a useful tool to design in first approximation the wells of an optimal QCD.

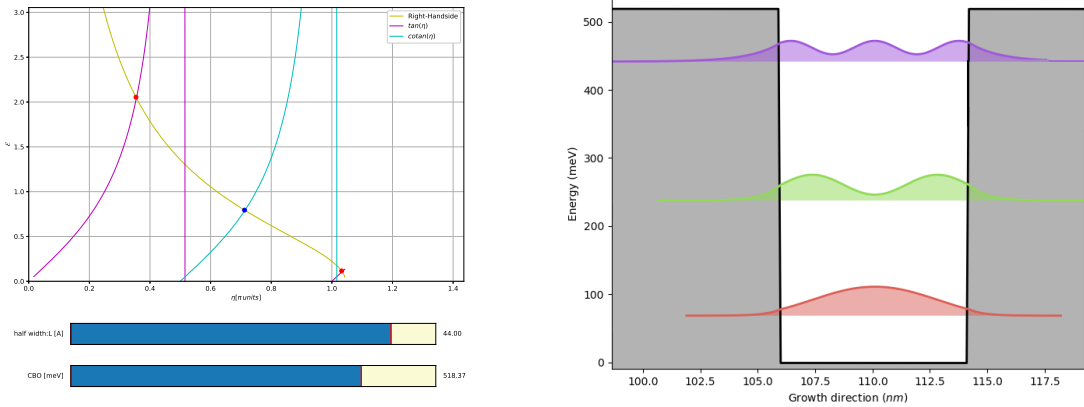


**Figure A.1:** (a) Graphical representation of the computation to obtain the energy levels in a finite quantum well and (b) relative states.

# Bibliography

- [1] Laure Gendron, M Carras, Agnès Huynh, V Ortiz, C Koeniguer, and V Berger. Quantum cascade photodetector. *Applied physics letters*, 85(14):2824–2826, 2004.
- [2] Daniel Hofstetter, Mattias Beck, and Jérôme Faist. Quantum-cascade-laser structures as photodetectors. *Applied Physics Letters*, 81(15):2683–2685, 2002.
- [3] Daniel Hofstetter, Fabrizio R Giorgetta, Esther Baumann, Quankui Yang, Christian Manz, and Klaus Köhler. Midinfrared quantum cascade detector with a spectrally broad response. *Applied Physics Letters*, 93(22):221106, 2008.
- [4] Shen-Qiang Zhai, Jun-Qi Liu, Feng-Qi Liu, and Zhan-Guo Wang. A normal incident quantum cascade detector enhanced by surface plasmons. *Applied Physics Letters*, 100(18):181104, 2012.
- [5] Tatsuo Dougakiuchi, Kazuue Fujita, Toru Hirohata, Akio Ito, Masahiro Hitaka, and Tadataka Edamura. High photoresponse in room temperature quantum cascade detector based on coupled quantum well design. *Applied Physics Letters*, 109(26):261107, 2016.
- [6] Peter Reininger, Benedikt Schwarz, Hermann Detz, Don MacFarland, Tobias Zederbauer, Aaron Maxwell Andrews, Werner Schrenk, Oskar Baumgartner, Hans Kosina, and Gottfried Strasser. Diagonal-transition quantum cascade detector. *Applied Physics Letters*, 105(9):091108, 2014.
- [7] Alexandre Delga. Quantum cascade detectors: A review. In *Mid-infrared Optoelectronics*, pages 337–377. Elsevier, 2020.
- [8] Alexandre Delga, Laetitia Doyennette, Vincent Berger, Mathieu Carras, Virginie Trinité, and Alexandru Nedelcu. Performances of quantum cascade detectors. *Infrared Physics & Technology*, 59:100–107, 2013.
- [9] Alexandre Delga and Luc Leviandier. Free-space optical communications with quantum cascade lasers. In *Quantum Sensing and Nano Electronics and Photonics XVI*, volume 10926, page 1092617. International Society for Optics and Photonics, 2019.
- [10] Fabrizio R Giorgetta, Esther Baumann, Ricardo Théron, ML Pellaton, Daniel Hofstetter, M Fischer, and Jérôme Faist. Short wavelength ( $4 \mu\text{m}$ ) quantum cascade detector based on strain compensated in ga as/ in al as. *Applied Physics Letters*, 92(12):121101, 2008.
- [11] Kong Ning, Liu Jun-Qi, Li Lu, Liu Feng-Qi, Wang Li-Jun, and Wang Zhan-Guo. Strain-compensated ingaas/inalas quantum cascade detector of  $4.5 \mu\text{m}$  operating at room temperature. *Chinese Physics Letters*, 27(3):038501, 2010.
- [12] Wang Xuejiao, Liu Junqi, Zhai Shenqiang, Liu Fengqi, and Wang Zhanguo. Room temperature quantum cascade detector operating at  $4.3 \mu\text{m}$ . *Journal of Semiconductors*, 35(10):104009, 2014.
- [13] Marcel Graf. *Design and characterisation of far-and mid-infrared quantum cascade detectors*. PhD thesis, Université de Neuchâtel, 2008.

- [14] Gerald Bastard et al. Wave mechanics applied to semiconductor heterostructures. 1988.
- [15] Danièle Palaferri. *Antenna resonators for quantum infrared detectors and fast heterodyne receivers*. PhD thesis, Sorbonne Paris Cité, 2018.
- [16] Marcel Graf, Nicolas Hoyler, Marcella Giovannini, Jérôme Faist, and Daniel Hofstetter. Inp-based quantum cascade detectors in the mid-infrared. *Applied physics letters*, 88(24):241118, 2006.
- [17] C Koeniguer, G Dubois, A Gomez, and V Berger. Electronic transport in quantum cascade structures. *arXiv preprint cond-mat/0610373*, 2006.
- [18] Paul R Thompson and Thomas C Larason. Method of measuring shunt resistance in photodiodes. In *Measurement Science Conference*, volume 400, 2001.
- [19] Benedikt Schwarz, Peter Reininger, Hermann Detz, Tobias Zederbauer, Aaron Maxwell Andrews, Stefan Kalchmair, Werner Schrenk, Oskar Baumgartner, Hans Kosina, and Gottfried Strasser. A bi-functional quantum cascade device for same-frequency lasing and detection. *Applied Physics Letters*, 101(19):191109, 2012.
- [20] A Harrer, B Schwarz, S Schuler, P Reininger, A Wirthmüller, H Detz, D Macfarland, T Zederbauer, AM Andrews, M Rothermund, et al. 4.3  $\mu\text{m}$  quantum cascade detector in pixel configuration. *Optics express*, 24(15):17041–17049, 2016.
- [21] Benedikt Schwarz, Peter Reininger, Andreas Harrer, Donald MacFarland, Hermann Detz, Aaron M Andrews, Werner Schrenk, and Gottfried Strasser. The limit of quantum cascade detectors: A single period device. *Applied Physics Letters*, 111(6):061107, 2017.